



Efficient CO₂ reduction under visible light: Synergistic effects of Cu nanoparticles and Ni single atoms

Wei-guo Pan^{a,b,c}, Chu-fan Li^a, Zhen-rui Zhang^a, Tong Wu^a, Rui-tang Guo^{a,b,c,*}

^a College of Energy and Mechanical Engineering, Shanghai University of Electric Power, Shanghai 200090, People's Republic of China

^b Shanghai Non-Carbon Energy Conversion and Utilization Institute, Shanghai 200090, People's Republic of China

^c Key Laboratory of Environmental Protection Technology for Clean Power Generation in Machinery Industry, Shanghai 200090, People's Republic of China

ARTICLE INFO

Keywords:

CO₂ reduction
Single-atom photocatalysts
ZIF-8
Nitrogen-doped carbon
And C₂H₆

ABSTRACT

Photocatalytic reduction of CO₂ is a considerable method to alleviate global warming and energy shortage. In this work, CoAl-LDH/Ni₁Cu_{NP} nitrogen-doped carbon composites (CA/Ni₁Cu_{NP} N-C) can efficiently reduce CO₂ into CO, CH₄, and C₂H₆ under visible light. In situ characterization techniques and theoretical calculations were employed to investigate the CO₂ evolution pathway and photocatalytic mechanism. The synergistic interaction of Cu nanoparticles and Ni single-atom sites accelerated the photogenerated charge separation and facilitated the adsorption properties of key intermediates. As a result, the yields of CH₄ and C₂H₆ on CA/Ni₁Cu_{NP} N-C were achieved up to 35.245 and 25.328 μmol g⁻¹ h⁻¹ with electron selectivity of 40.24% and 50.61%, respectively. This work is instructive for using metal nanoparticles to optimize single-atom catalysts to promote their catalytic activity.

1. Introduction

The massive carbon dioxide (CO₂) emissions have led to drastic climate changes and frequent extreme natural disasters. Reducing CO₂ into value-added fuels and chemicals by artificial photosynthesis is a promising solution to environmental problems and energy crises. [1,2] In recent years, some semiconductor materials and reaction systems with superior photocatalytic properties have been developed, and significant progress has been made in energy conversion efficiency, operational stability, and product selectivity. [3–5] Photocatalytic reduction of CO₂ into CO and HCOOH is kinetically favorable because their generation requires the transfer of only 2 electrons. However, converting CO₂ into products with higher economic value is very difficult. For example, the generation of CH₄ is thermodynamically favorable, but its evolution involves the adsorption of *CO intermediates and 8-electron transfer, which are kinetically challenging. On this basis, the generation of C₂H₆ further involves the rate-determining step (RDS) of C-C coupling and more hydrogenation reactions. [6–8] Therefore, designing novel photocatalysts with high carrier separation efficiency, moderate intermediate adsorption capacity, and sufficient active sites is of great significance for generating high-value products.

Narrowing the scale of conventional bulk materials to nanoparticles,

clusters, or even single atoms can exponentially increase the number of active sites. [9] In particular, single-atom catalysts theoretically possess 100% utilization since they are well dispersed on the atomic scale. [10] In addition, isolated single-atom sites have unique electronic structures and coordination environments, which are favorable for CO₂ catalytic reduction with complex reaction pathways. [11,12] The zeolite imidazole framework-8 (ZIF-8) formed by the coordination of Zn²⁺ and 2-methylimidazole is one of the classical metal-organic frameworks (MOFs) with a well-defined coordination pattern and dispersed pore structure. [13] Therefore, ZIF-8 is an ideal precursor for designing controllable morphology and functionalized catalysts. Substituting a portion of Zn²⁺ based on the metal ion exchange strategy can obtain atomically isolated metal-doped species (M), which is a mature technology for anchoring metal single atoms on ZIF-8-derived nitrogen-doped carbon (N-C). [14] Since N atoms tend to establish strong electron-metal-carrier interactions (EMCIs) with metal species, it can effectively anchor metal atoms and maintain their atomic dispersion at high temperatures. [15] In addition, the ZIF-8-derived single-atom catalyst inherits its special pore structure and possesses superior electrical conductivity, which is favorable for the adsorption of reactants/intermediates and rapid charge migration, and thus it has been widely studied in energy and environmental catalysis. [16–18]

* Corresponding author at: College of Energy and Mechanical Engineering, Shanghai University of Electric Power, Shanghai 200090, People's Republic of China.
E-mail address: guta@sohu.com (R.-t. Guo).

<https://doi.org/10.1016/j.apcatb.2023.123492>

Received 20 September 2023; Received in revised form 22 October 2023; Accepted 6 November 2023

Available online 7 November 2023

0926-3373/© 2023 Elsevier B.V. All rights reserved.

However, the typical M-N₄ coordination has a symmetric electronic structure, which is not conducive to efficient carrier separation and C-C coupling. [19–21] The microenvironment of the active center can be modulated by doping elements, adjusting the coordination mode, and designing double single-atom sites, thus facilitating the conversion of CO₂ to CH₄ and C₂H₆. [22–24] Recently, several reports have found that metal nanoparticles coexisting with single atoms exhibit better catalytic performance than their individual components. [25–28] The introduction of metal nanoparticles creates new electron-rich centers, which can significantly change the charge distribution of the original single-atom sites. The establishment of the electron density difference can promote the separation of carriers and the aggregation of electrons. Meanwhile, the asymmetric charge densities around single-atom sites facilitates the coupling of *CO intermediates to promote the generation of multi-carbon products [20,29].

However, direct use of metal nanoparticle-single atom synergistic system based on N-C for photocatalytic CO₂ reduction is undesirable, due to the limitation of available photogenerated carriers. Adopting mature photocatalytic materials as photogenerated carrier sources and constructing heterojunctions with N-C can provide sufficient electrons to promote the catalytic reduction of CO₂. Layered double hydroxides (LDHs) with unique structures and good adsorption properties have been widely studied in non-homogeneous photocatalytic reaction systems. [30–32] Particularly, Co²⁺ in CoAl-LDH can accelerate the dissociation of H₂O thus promoting the catalytic reduction of CO₂. [33] However, CoAl-LDH-based photocatalysts tend to exhibit poor energy conversion efficiency due to the rapid recombination of photogenerated carriers and the lack of active sites. [34,35] CoAl-LDH and ZIF-8-derived N-C have adaptable energy-band structures, and hybridizing them can promote the transfer of photogenerated carriers to N-C. Meanwhile, the abundant active sites on N-C can efficiently reduce CO₂ under sufficient electron flow.

In this work, we anchored Cu nanoparticles and Ni single-atom sites on N-C (Ni₁Cu_{NP} N-C), which were then hybridized with CoAl-LDH (CA) by ultrasonic self-assembly method to obtain CoAl-LDH/Ni₁Cu_{NP} N-C (CA/Ni₁Cu_{NP} N-C) composites for photocatalytic CO₂ reduction. The yields of CH₄, CO, and C₂H₆ were 35.245, 32.067, and 25.328 μmol g⁻¹ h⁻¹, respectively, and their electron selectivity were 40.24%, 9.15%, and 50.61%, respectively. The product generation pathways, charge transfer mechanisms, and synergistic effects between Cu nanoparticles and Ni single-atom sites were investigated by in situ characterization techniques and DFT calculations. The atomically dispersed Ni single-atom sites provide sufficient active sites for the photocatalytic reaction. The loading of Cu nanoparticles establishes electron-rich centers that accelerate charge separation and transport. In addition, it also optimizes the electronic structure of the Ni center, which promotes the adsorption properties of the key intermediates and the C-C coupling step.

2. Results and discussion

2.1. Synthesis and characterization

Based on the conventional ZIF-8 preparation process, a certain amount of Cu²⁺ and Ni²⁺ was substituted for Zn²⁺ (the molar ratio of (Cu²⁺+Ni²⁺)/Zn²⁺ is 5%) to obtain NiCu@ZIF-8. Subsequently, ZIF-8-derived N-C with Cu nanoparticles and Ni single-atom sites (Ni₁Cu_{NP} N-C) was obtained by one-step pyrolysis under a nitrogen atmosphere. CoAl-LDH (CA) was prepared by a hydrothermal method, and the CA/Ni₁Cu_{NP} N-C composite catalyst was synthesized via ultrasonic self-assembly. For comparison tests, ZIF-8, Cu@ZIF-8, and Ni@ZIF-8 were synthesized and the corresponding N-C-based materials (M N-C) were obtained in the temperature range of 800–950 °C. Finally, a series of composite catalysts were synthesized by controlling the ratio of CA and M N-C (CA/M N-C).

The crystal structure of the as-prepared sample was studied by

powder X-ray diffraction (XRD). As shown in Fig. 1a, the diffraction peaks of pristine ZIF-8 at 10.46°, 12.8°, 14.78°, 16.52°, 18.1°, 22.22°, 24.58°, and 26.76° correspond to its (002), (112), (022), (013), (222), (114), (233), and (134) crystal faces, respectively. [36,37] These typical crystal surfaces verify the successful preparation of ZIF-8. Cu@ZIF-8, Ni@ZIF-8, and CuNi@ZIF-8 also exhibit diffraction peaks consistent with those of ZIF-8, which implies that the stabilized structure of ZIF-8 is preserved during the metal-ion exchange process. However, the diffraction peaks associated with the elements Cu and Ni are not detected due to their excessively low content and atomic dispersion. The optimal N-C, Cu_{NP} N-C, and Ni₁Cu_{NP} N-C were obtained by calcination under nitrogen atmosphere at 950 °C. As shown in Fig. 1b, the broad diffraction peaks near 23.34° and 43.54° correspond to the (002) and (101) facets of amorphous carbon. [38] For Cu_{NP} N-C, three distinct characteristic peaks at 13.14°, 50.32°, and 74.06° correspond to the (111), (200), and (220) crystal faces of Cu⁰, respectively. [39] The diffraction information of Ni₁Cu_{NP} N-C is similar to that of Cu_{NP} N-C. In particular, no Ni signal is detected on Ni₁Cu_{NP} N-C, which implies the atomic dispersion of Ni. The Ni₁Cu_{NP} N-C obtained at 800, 850, and 900 °C also exhibit similar diffraction information. As shown in Fig. S1, the characteristic peaks of Cu species are gradually enhanced with increasing temperature, which implies that high temperature is more favorable for Cu aggregation. The characteristic (003), (006), (009), (012), (018), (110), and (113) crystal faces of CA can be observed in its XRD pattern. [40,41] In addition, the diffraction peaks of each monomer are successfully detected on CA/Ni₁Cu_{NP} N-C (Fig. 1c), which means that the composite catalyst is successfully synthesized by ultrasonic self-assembly method.

The vibrational properties of N-C, Cu_{NP} N-C, Ni₁ N-C, and Ni₁Cu_{NP} N-C were investigated via Raman spectroscopy. As shown in Fig. 1d, all the samples exhibit distinct broad peaks near 1350 and 1580 cm⁻¹, which correspond to the C-atom lattice defects (D-band) and the phase crystalline graphite (G-band), respectively. The peak intensity ratio of the D and G bands (I_D/I_G) can evaluate the degree of graphitization. It is obvious that doping metal is conducive to improving the crystal quality of N-C, thus obtaining better photoelectron transport efficiency. [42,43] The specific surface area and pore size of catalysts play an essential role in the mass transfer of reactants and adsorption of key intermediates during heterogeneous reaction. [44] Therefore, the pore structure of the as-prepared samples was investigated by nitrogen absorption measurements (Fig. S2 and Table S1). Compared to CA (55.435 m² g⁻¹), CuNi@ZIF-8 has a larger Brunauer-Emmett-Teller (BET) surface area (1113.903 m² g⁻¹), which is attributed to the unique mesoporous structure of ZIF-8. After pyrolysis, the specific surface area of Ni₁Cu_{NP} N-C decreases dramatically (479.938 m² g⁻¹) due to the collapse of the carbon structure and the formation of defects. [45] As the low content of CA, CA/Ni₁Cu_{NP} N-C possesses a similar specific surface area (427.907 m² g⁻¹) and pore size as Ni₁Cu_{NP} N-C.

The microstructure of the as-prepared samples was investigated by scanning electron microscopy (SEM), transmission electron microscopy (TEM), high-resolution transmission electron microscopy (HR-TEM), energy dispersive spectrometer (EDS), and high-angle annular darkfield scanning transmission electron microscopy (HAADF-STEM). As shown in Fig. 2a, CA exhibits a nanoflower-like shape formed by the aggregation of 2D nanosheets. The structure of CA is relatively loose, and some smaller nanosheets are attached to its surface (Fig. S3a and Fig. 2b). N-C transformed from pure ZIF-8 exhibits a rhombic dodecahedral structure. Due to the reduction and evaporation of Zn and the disappearance of organic ligands at high temperatures, N-C presents a rough surface. [46] In particular, some N-C particles directly expose their internal coral-like skeleton and no longer have an intact surface (Fig. S3b and Fig. S4). After being loaded with Cu and Ni, a few uniformly distributed nanoparticles are observed on the N-C (Fig. 3a and Fig. S3c), and the EDS results confirmed that they are Cu nanoparticles formed by the reduction and aggregation of Cu²⁺ at high temperature (Fig. S5). Correspondingly, the Ni element is spatially uniformly dispersed, which implies that Ni

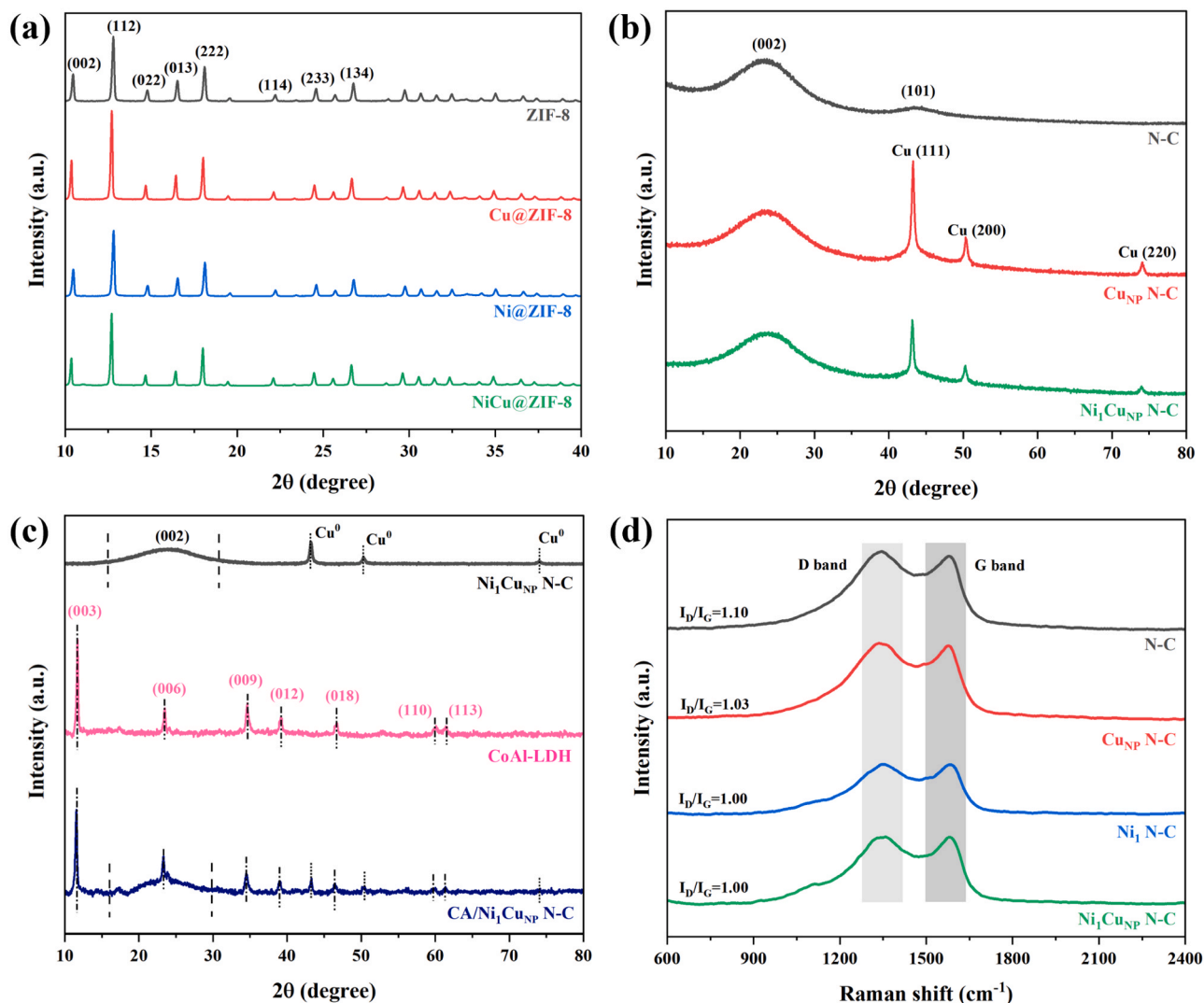


Fig. 1. The XRD patterns of (a) ZIF-8, Cu@ZIF-8, Ni@ZIF-8, and CuNi@ZIF-8. (b) N-C, CuNP N-C, and Ni₁CuNP N-C. (c) Ni₁CuNP N-C, CoAl-LDH, and CA/Ni₁CuNP N-C. The Raman spectra of N-C, CuNP N-C, Ni₁ N-C, and Ni₁CuNP N-C.

was successfully embedded into N-C as single-atom sites. The carbon products evolved from CuNi@ZIF-8 show a more regular dodecahedral structure (Fig. 2c-d). The TEM images of Ni₁CuNP N-C also show that some regular cyclic graphitized carbon is formed at the edge of the N-C. The HR-TEM (Fig. 3c) and HAADF-STEM (Fig. S6) images of Ni₁CuNP N-C show that the lattice gap of the nanoparticles is about 0.208 nm, which corresponds to the (111) crystal faces of Cu⁰. [41] Since metallic Cu can promote carbon evolution, the Cu nanoparticles are uniformly encapsulated by graphitized carbon (layer spacing is approximately 0.34 nm) to form a unique core-shell structure. The carbon layer with superior electrical conductivity can promote the rapid migration of electrons to active sites, which is favorable for the CO₂ reduction reaction with multi-electron participation. [47,48] For CA/Ni₁CuNP N-C composite catalysts, CA is dispersed into nanosheets and rosette-like structures after sonication and distributed in the interstitials of Ni₁CuNP N-C (Fig. 2e-f and Fig. S3d). Its EDS mapping photos are similar to those of Ni₁CuNP N-C, which suggests that sonication did not change its surface metal dispersion state (Fig. S7). In addition, HAADF-STEM image analysis further confirmed the atomic dispersion of Ni on CA/Ni₁CuNP N-C, and these isolated Ni sites are highlighted by red circles (Fig. 3d).

The surface element composition and chemical state of the samples were determined by X-ray photoelectron spectroscopy (XPS). The survey

XPS spectra of CA, Ni₁CuNP N-C, and CA/Ni₁CuNP N-C are shown in Fig. S8. Due to the low content of Ni and Cu, no obvious characteristic peaks belonging to them are detected in the survey spectra. The spin-orbit double peaks belonging to Co 2p_{3/2} (781.22 eV) and Co 2p_{1/2} (797.36 eV) and the corresponding satellite peaks located at 787.24 and 804.04 eV can be detected in the pristine CA HR-XPS Co 2p spectrum (Fig. S9a). The characteristic peak located near 74.39 eV in the Al 2p spectrum (Fig. S9b) indicates the presence of Al³⁺. [41] The HR-XPS spectra of Co, Al, C, N, Ni, and Cu elements in CA/Ni₁CuNP N-C are shown in Fig. 4. Compared with the pristine CA, the positions of the corresponding characteristic peaks of Co 2p and Al 2p are shifted toward the direction of high binding energy, which indicates that the electron cloud density of this component decreases and electrons are more inclined to migrate to Ni₁CuNP N-C. [40] In the HR-XPS C 1s spectrum of CA/Ni₁CuNP N-C, the peaks located at 284.77, 285.87, and 288.69 eV correspond to C-C, C=N, and N-C bonds, respectively. [49] The peaks located at 398.62, 399.36, 400.85, 402.09, and 404.62 eV belong to pyridinic N, Ni-N, pyrrolic N, graphitic N, and oxidized N, respectively, which is consistent with the pristine Ni₁CuNP N-C (Fig. S10). [50,51] Functionalized pyridine N can act as a coordination center to anchor metal single atoms. In addition, the presence of Ni-N bonds implies the existence of isolated Ni single atoms and coordination with N. [52] The characteristic peak belonging to Ni 2p_{3/2} (854.92 eV) is between Ni⁰

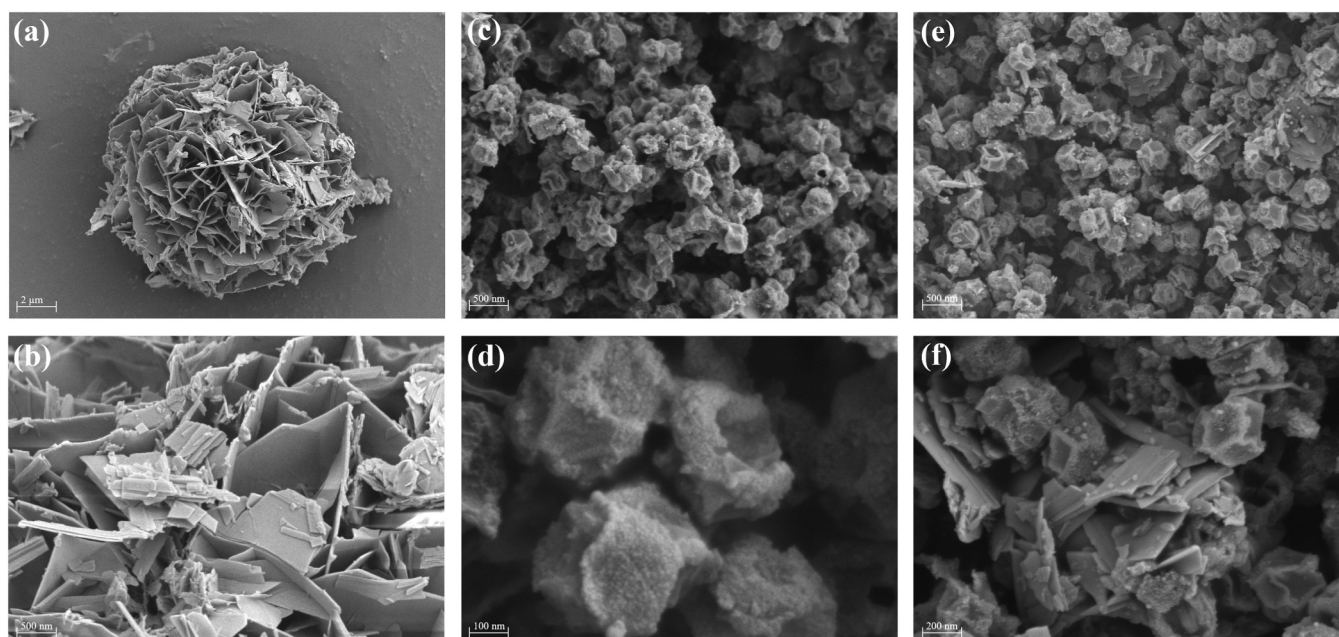


Fig. 2. The SEM images of (a-b) CoAl-LDH, (c-d) Ni₁CuNP N-C, and (e-f) CA/Ni₁CuNP N-C.

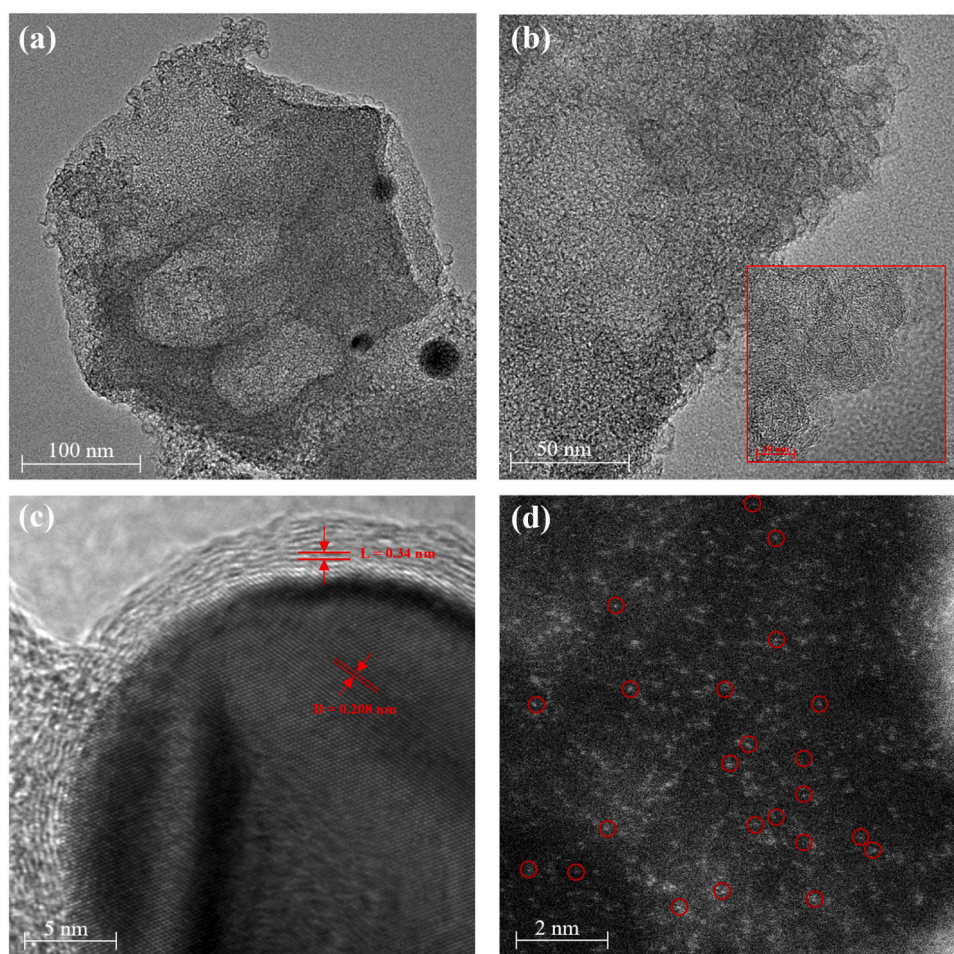


Fig. 3. The TEM images of (a-b) Ni₁CuNP N-C. (c) The HR-TEM image of Ni₁CuNP N-C. (d) The HAADF-STEM image of CA/Ni₁CuNP N-C.

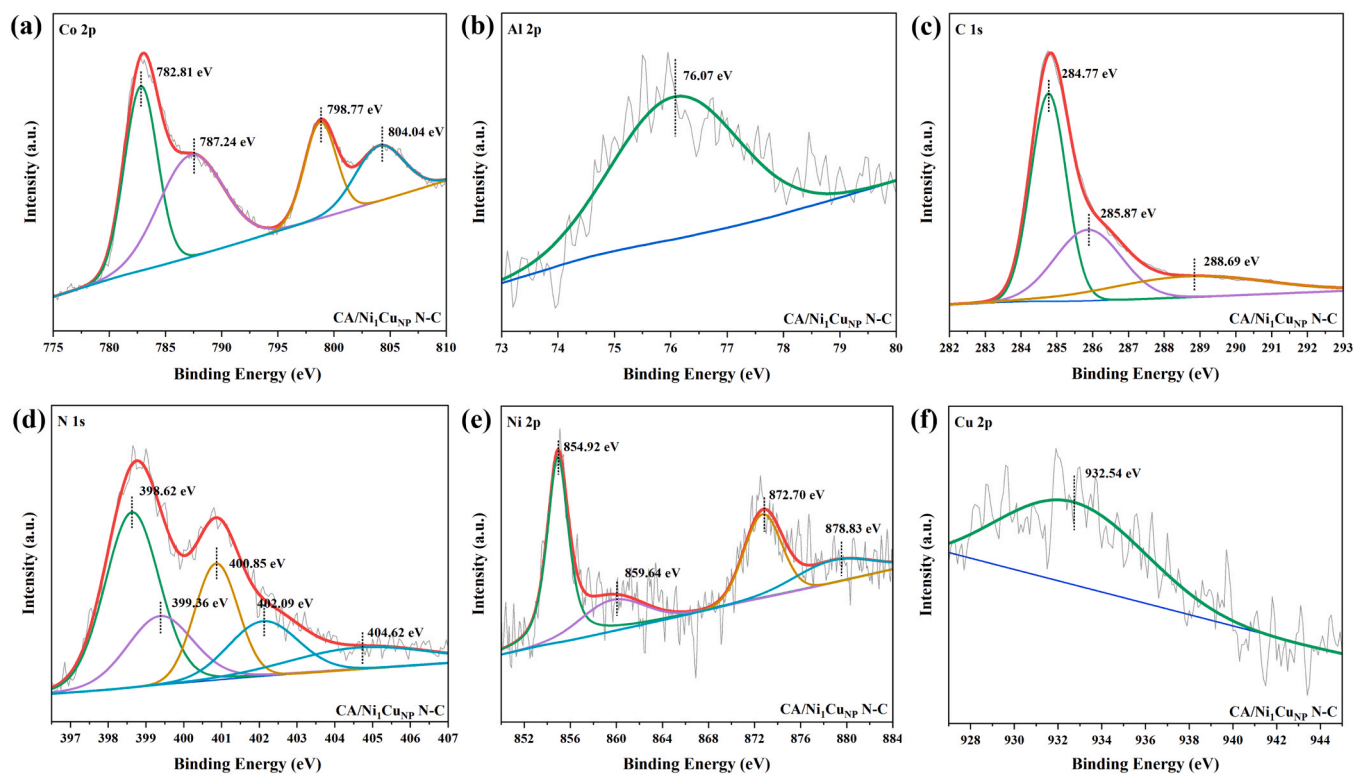


Fig. 4. The (a) Co 2p, (b) Al 2p, (c) C 1s, (d) N 1s, (e) Ni 2p, and (f) Cu 2p HR-XPS images of CA/Ni₁Cu_{NP} N-C.

(852.9 eV) and Ni²⁺ (856.0 eV), which suggests that the valence state of Ni in the CA/Ni₁Cu_{NP} N-C is between 0 and + 2. [53] As shown in Fig. 4f, the single peak detected near 932.54 eV belongs to Cu⁰ 2p_{3/2}. [54] No

signals regarding Cu⁺ and Cu²⁺ are detected indicating that elemental Cu is mainly present in the form of Cu nanoparticles.

The electronic structure and coordination environment of Ni in CA/

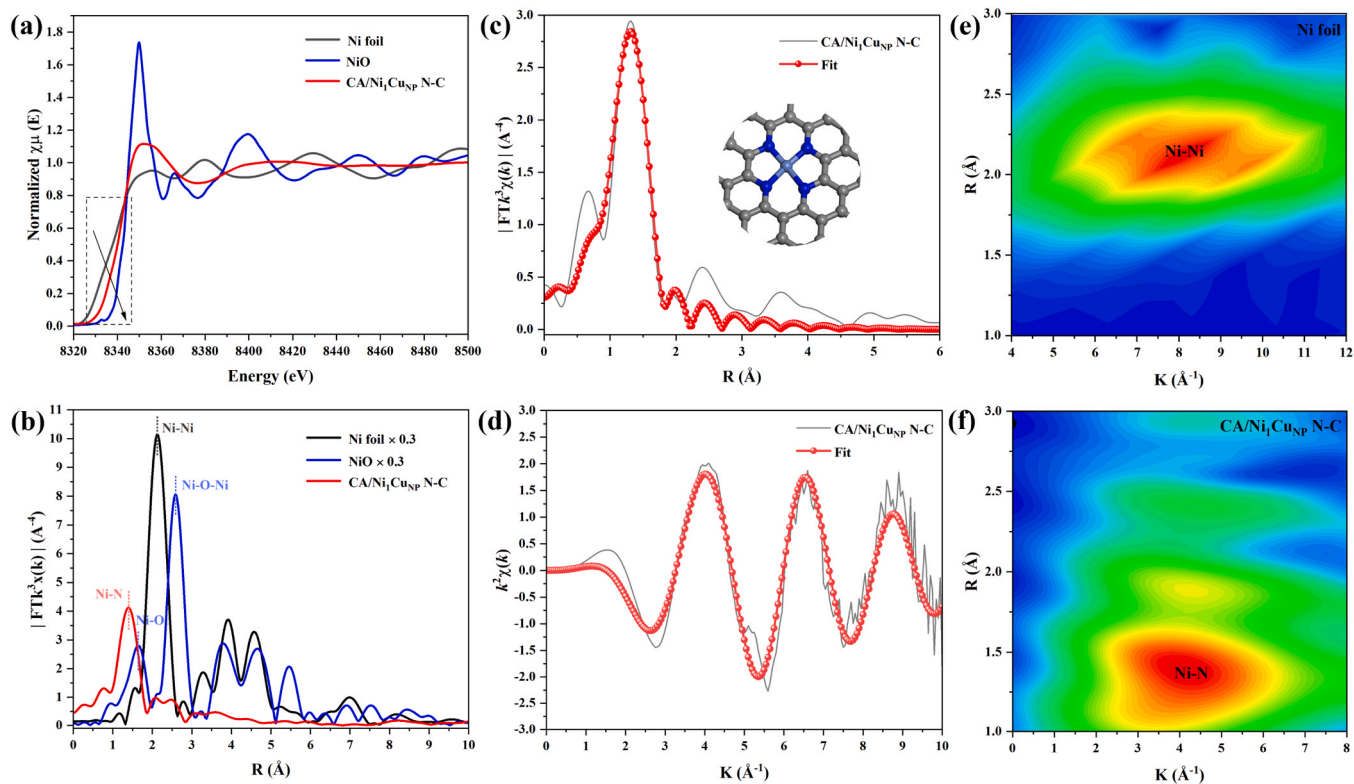


Fig. 5. The (a) Ni K-edge XANES and (b) FT k^3 -weighted EXAFS spectra of CA/Ni₁Cu_{NP} N-C and the reference samples. The FT-EXAFS fitting curve of CA/Ni₁Cu_{NP} N-C in (c) R-space (inset shows the proposed NiN₄ coordination environment) and (d) k-space. The WT-EXAFS signals of (e) Ni foil and (f) CA/Ni₁Cu_{NP} N-C.

Ni₁Cu_{NP} N-C were further confirmed by Ni K-edge X-ray absorption near edge structure (XANES) and extended X-ray absorption fine structure (EXAFS) characterization. As shown in Fig. 5a, the energy absorption edge of CA/Ni₁Cu_{NP} N-C is located between the standard Ni foil and NiO, which indicates that the valence state of Ni in CA/Ni₁Cu_{NP} N-C is between 0 and +2, which is consistent with the analysis results of XPS. As shown in Fig. 5b, no peaks associated with the Ni-Ni bond (2.12 Å), Ni-O-Ni bond (2.58 Å), and Ni-O bond (1.66 Å) are detected in the Fourier-transformed (FT) Ni k³-weighted EXAFS spectra, which indicates the absence of Ni nanoparticles and Ni oxides. Correspondingly, a characteristic peak associated with the scattering path of the Ni-N bond (1.41 Å) is detected in CA/Ni₁Cu_{NP} N-C, which suggests that the Ni in CA/Ni₁Cu_{NP} N-C is mainly in the Ni-N_X configuration similar to nickel phthalocyanine (Ni pc). [37] In addition, the Wavelet transform (WT) Ni K-edge EXAFS results (Fig. 5e-f) show that the intensity maximum of CA/Ni₁Cu_{NP} N-C in k-space is located at 4.07 Å⁻¹ without a correlation signal about the Ni-Ni coordination (9.08 Å⁻¹) in Ni foils, which further confirms that the atomic dispersion of Ni. Based on the EXAFS fitting results, the coordination number X was determined to be about 3.6, and it can be assumed that the Ni atoms in the CA/Ni₁Cu_{NP} N-C are coordinated to four N atoms and have a bond length of about 1.86 Å (Fig. 5c-d and Table S2).

2.2. Optical and photoelectrochemical properties

The light-absorbing ability of the photocatalyst is an essential index for evaluating its performance. As shown in Fig. 6a, CA has two distinct absorption bands in the UV and visible regions. [41] The black N-C, Cu_{NP} N-C, Ni₁ N-C, and Ni₁Cu_{NP} N-C exhibit superior light absorption in the UV and visible ranges, with an absorption edge of about 700 nm (Fig. S11). It is noteworthy that the light-absorbing ability of Cu_{NP} N-C and Ni₁Cu_{NP} N-C in the near-infrared region (NIR) is also significantly enhanced compared to N-C and Ni₁ N-C, which may be attributed to the localized surface plasmon resonance (LSPR) effect induced by the Cu nanoparticles. The CA/Cu_{NP} N-C, CA/Ni₁ N-C, and CA/Ni₁Cu_{NP} N-C composites exhibit similar light-absorbing properties as those of the

corresponding M N-C-based materials due to the lower content of CA. As shown in Fig. 6b, the band gap (*E_g*) energies of CA, Ni₁Cu_{NP} N-C, and CA/Ni₁Cu_{NP} N-C are calculated as 3.41, 2.42, and 2.49 eV, respectively.

Electrochemical impedance spectroscopy (EIS) and transient photocurrent response (TPR) measurements were used to further investigate the charge transfer resistance and photocarrier separation efficiency of the prepared samples. The radius of the arc in the Nyquist diagram directly reflects the charge transfer resistance (*R_{ct}*) of the samples, and it is clear that the composite CA/Ni₁Cu_{NP} N-C has the smallest *R_{ct}* (Fig. 6e). By further fitting the test results, the *R_{ct}* of CA, CA/Cu_{NP} N-C, CA/Ni₁ N-C, and CA/Ni₁Cu_{NP} N-C are 4169, 464.5, 250.6, and 42.89 Ω, respectively (Table S3). As shown in Fig. 6d, the original CA exhibits a small photocurrent density, meaning that many carriers recombine during migration. Correspondingly, the transient photocurrents of CA/Cu_{NP} N-C, CA/Ni₁ N-C, and CA/Ni₁Cu_{NP} N-C composites are significantly increased, which means that the hybrid of M N-C based materials and CA can substantially improve the photogenerated charge transport and separation mechanism. In the photoluminescence (PL) spectrum (Fig. 6e), CA exhibits the strongest peak near 420 nm, which is a fluorescence effect caused by the large number of recombination carriers during the transition. The fluorescence intensities of the composite samples are all reduced and the CA/Ni₁Cu_{NP} N-C has a minor fluorescence peak, further confirming its superior carrier separation efficiency. According to the time-resolved photoluminescence (TRPL) attenuation spectrum, the average carrier lifetime (Table S4) of CA, CA/Cu_{NP} N-C, CA/Ni₁ N-C, and CA/Ni₁Cu_{NP} N-C are 27.18, 29.99, 33.37, and 38.91 ns, respectively. The optimal carrier separation and transport properties of CA/Ni₁Cu_{NP} N-C may be due to the asymmetric electron density formed on the carbon substrate by the interaction of Ni₁ and Cu_{NP}. [15,55] Therefore, CA/Ni₁Cu_{NP} N-C can produce more valuable carriers to participate in the CO₂ reduction reaction, promoting the formation of long carbon chain products involving multiple electron transfer.

2.3. Photocatalytic CO₂ reduction performance

A series of Ni₁Cu_{NP} N-C were prepared in the range of 800–950 °C

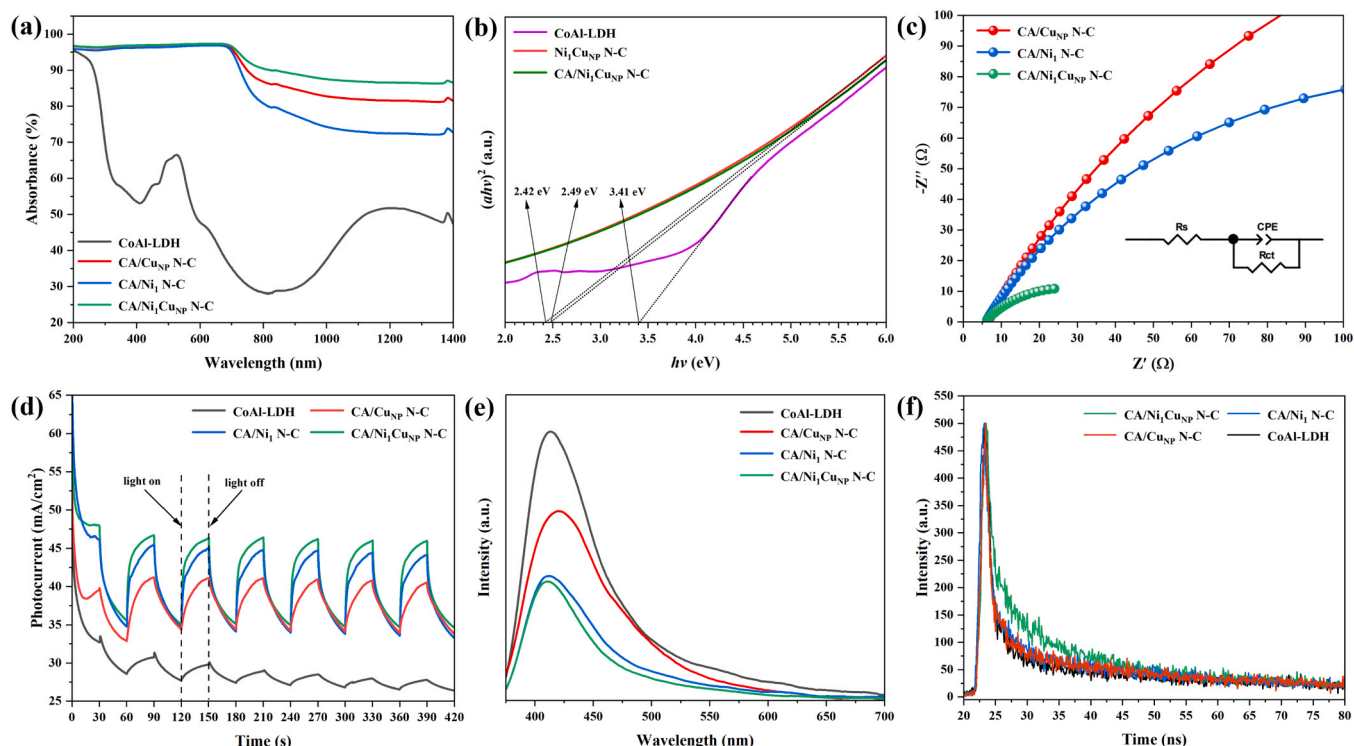


Fig. 6. The (a) UV-Vis-NIR absorption spectra, (b) Tauc plots, (c) EIS, (d) TPR, (e) PL, and (f) TRPL tests of as-prepared samples.

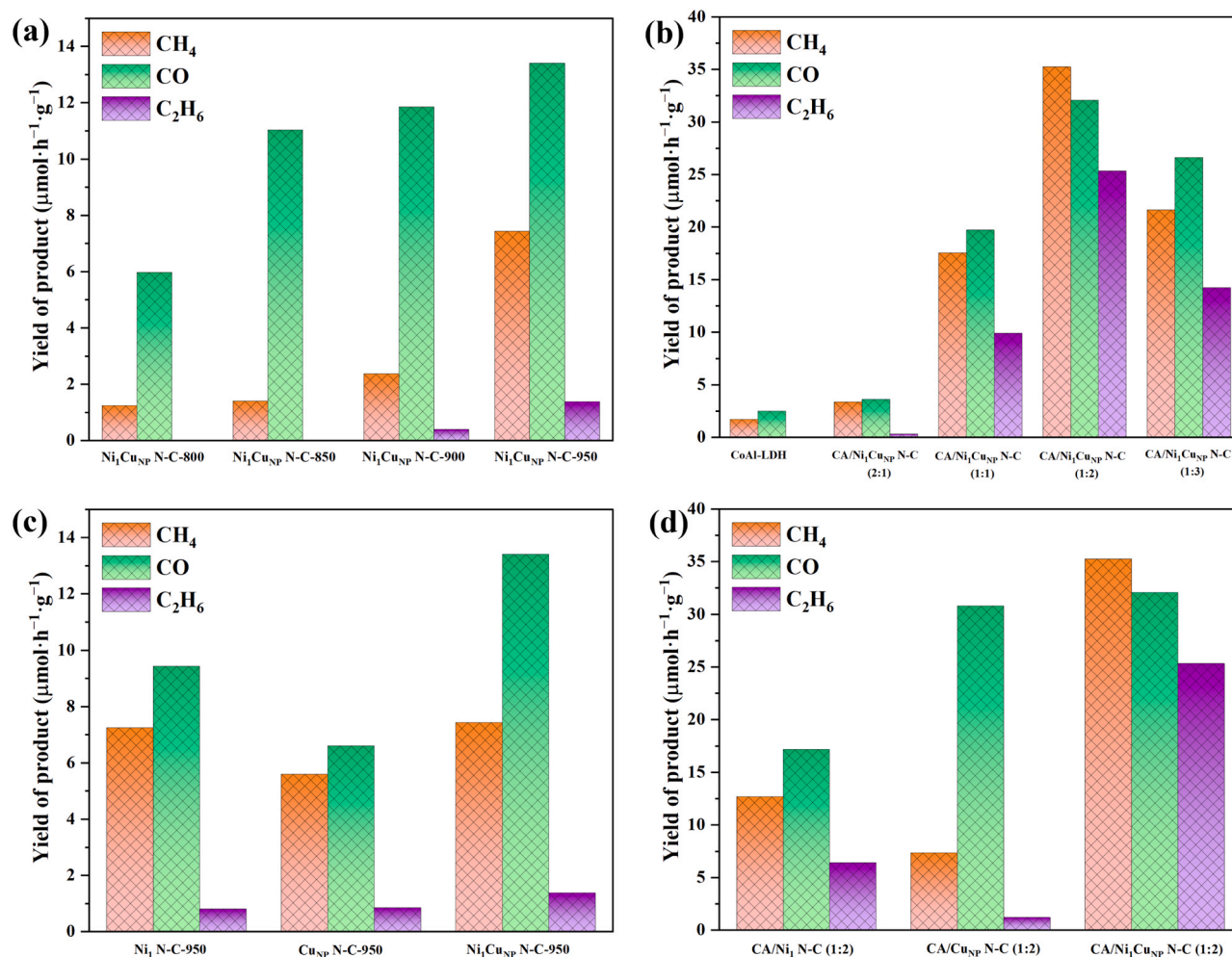


Fig. 7. The photocatalytic CO_2 reduction performance of as-prepared samples under visible light.

under the N_2 atmosphere to investigate the effect of calcination temperature on their photocatalytic performance. As shown in Fig. 7a, the photocatalytic performance of $\text{Ni}_1\text{CuNP N-C}$ is enhanced with increasing calcination temperature. In particular, $\text{Ni}_1\text{CuNP N-C-900}$ and $\text{Ni}_1\text{CuNP N-C-950}$ can reduce CO_2 into C_2H_6 . Higher temperatures can activate electron-metal-supporter interactions (EMSIs), when anchoring metal single atoms on N-C derived from ZIF-8 based on ion exchange strategies. This strong interaction is conducive to the coordination of metal ions and N sites. [15] In addition, the higher calcination temperature can ensure that the Zn species in the original ZIF-8 are fully evaporated, thus obtaining the target coordination pattern. $\text{Ni}_1\text{CuNP N-C-950}$ and CA were hybridized in different proportions by ultrasonic self-assembly method. Compared with the pristine CA, the photocatalytic activities of several $\text{CA/Ni}_1\text{CuNP N-C}$ composites are enhanced. As shown in Fig. 7b, the yields of CH_4 , CO , and C_2H_6 are increased with the percentage of $\text{Ni}_1\text{CuNP N-C}$ since it can provide more active sites. Moreover, the selectivity of C_2H_6 has also been significantly improved. Under visible light, the yields of CH_4 , CO , and C_2H_6 on $\text{CA/Ni}_1\text{CuNP N-C (1:2)}$ are 35.245, 32.067, and 25.328 $\mu\text{mol g}^{-1} \text{h}^{-1}$, respectively, and the electron selectivity of C_2H_6 is about 50.61%. It can be observed that the photocatalytic performance of the composites decreases significantly when the ratio of $\text{Ni}_1\text{CuNP N-C}$ is continuously increased. Although the black $\text{Ni}_1\text{CuNP N-C}$ can improve the light absorption and active site of the composite photocatalysts, most of the incident light is not converted into usable photogenerated carriers, but released into the surrounding environment as heat energy. Therefore, the lower content of CA leads to a decrease in the actual photogenerated carrier, which is the main

reason for the decrease in photocatalytic activity.

Then, we evaluated the photocatalytic CO_2 reduction performance of $\text{Ni}_1\text{ N-C-950}$, CuNP N-C-950 , and $\text{Ni}_1\text{CuNP N-C-950}$ under visible light to further investigate the synergistic effect of Ni single-atom sites and Cu nanoparticles. As shown in Fig. 7c, $\text{Ni}_1\text{CuNP N-C-950}$ exhibit the best photocatalytic activity, which implies that the interaction of Ni single atoms and Cu nanoparticles can promote CO_2 reduction. On CA/CuNP N-C , CO was the main gas-phase product due to the poor adsorption characteristics of the CuNP sites for *CO , so that *CO was easily desorbed on the catalyst surface. Correspondingly, $\text{CA/Ni}_1\text{ N-C}$ has higher CH_4 and C_2H_6 yields while the CO yield is significantly decreased. This implies that the dispersed Ni single-atom sites have better adsorption properties for *CO intermediates, thus favoring the subsequent hydrogenation reaction to generate multi-electron transfer products. In particular, $\text{CA/Ni}_1\text{CuNP N-C}$ show the best catalytic performance, which is attributed to the synergistic effect of Cu nanoparticles and Ni single atoms. The loading of Cu nanoparticles can establish electron-rich centers near the Ni single-atom sites to promote carrier separation and transport, thus obtaining sufficient electron sources to promote the CO_2 catalytic reduction reaction. On the other hand, establishing asymmetric Ni-N_4 active sites is conducive to C-C coupling, thus enabling the generation of C_2 products. Therefore, this synergistic effect can optimize the photogenerated carrier separation mechanism and promote C-C coupling, thus exhibiting enhanced photocatalytic activity and considerable CH_4 and C_2H_6 yields.

The isotope labeling tests were performed using $^{13}\text{CO}_2$ under the same test conditions, and the products were analyzed by gas

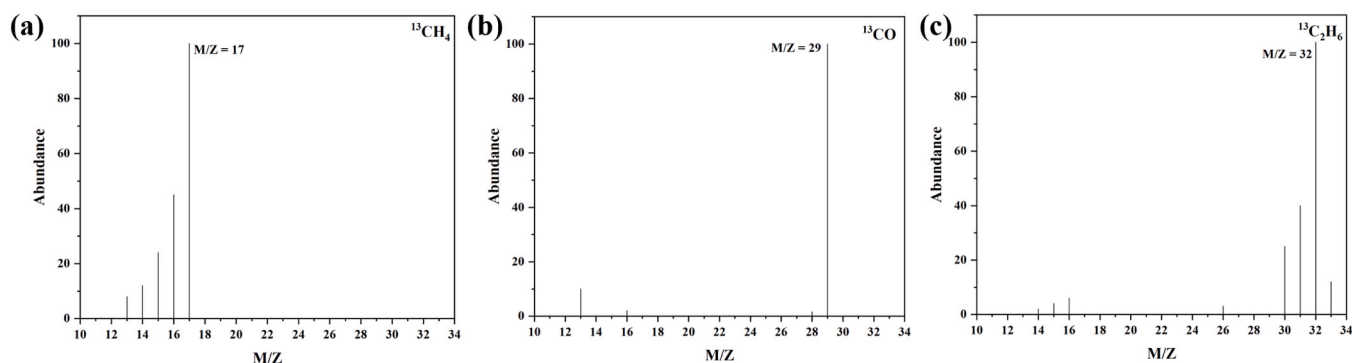


Fig. 8. GC-MS analysis for photocatalytic $^{13}\text{CO}_2$ reduction.

chromatography-mass (GC-MS) spectrometry. As shown in Fig. 8, the peaks located at $M/Z = 17$, 29 , and 32 corresponded to $^{13}\text{CH}_4$, ^{13}CO , and $^{13}\text{C}_2\text{H}_6$, respectively, which indicated that the products were all derived from CO_2 rather than carbon pollution. The durability of the photocatalyst is a vital evaluation index for its application value. As shown in Fig. S12, the CH_4 , CO , and C_2H_6 all exhibit stable generation rates under 10 h of continuous irradiation. There is no significant decrease in the photocatalytic activity of the best sample CA/ $\text{Ni}_1\text{Cu}_{\text{NP}}$ N-C after three cycle tests (30 h). The SEM image (Fig. S13) and XPS pattern (Fig. S14) of the CA/ $\text{Ni}_1\text{Cu}_{\text{NP}}$ N-C sample after cyclic testing further confirm its structural stability.

2.4. Mechanism of photocatalytic CO_2 reduction

The energy band structures (Fig. S15) of CA and N-C were determined based on the Mott-Schottky (Fig. S16) and Tauc plots. Under irradiation, the electrons located on the conduction band (CB) of CA will be transferred to the CB of N-C by the internal potential, and then converge to the Cu nanoparticles and Ni single-atom sites to participate in the reduction reaction. Correspondingly, holes located in the valence band (VB) of CoAl-LDH will transfer to the VB of N-C and finally be consumed by the sacrificial agent (TEOA).

The CO_2 -temperature programmed desorption (CO_2 -TPD) tests up to 500°C were carried out to further investigate the chemical adsorption properties of the prepared materials for CO_2 . As shown in Fig. S17, the best sample CA/ $\text{Ni}_1\text{Cu}_{\text{NP}}$ N-C exhibits more obvious desorption peaks than CA/ Cu_{NP} N-C at 127.3 , 338.5 , and 428.3°C , which directly proves that the introduction of Ni single atomic sites could obtain enhanced chemisorption properties of CO_2 . In addition, a slight shift of the moderately alkaline sites of CA/ $\text{Ni}_1\text{Cu}_{\text{NP}}$ N-C to higher temperatures also indicates the presence of more adsorption sites. For inferring the CO_2 evolution pathway, in situ Fourier transform infrared spectroscopy (FT-IR) was used to determine the type of intermediates adsorbed on the catalyst surface during the catalytic reduction process. As shown in Fig. S18, HCO_3^- (1417 cm^{-1}), b-CO_3^{2-} (1508 cm^{-1}), m-CO_3^{2-} (1555 cm^{-1}), and CO_2^- (1686 cm^{-1}) are detected on the surface of CA/ $\text{Ni}_1\text{Cu}_{\text{NP}}$ N-C after continuous purging of CO_2 and H_2O for 10 min under dark conditions. [56] These carbonates, bicarbonates, and CO_2 reactive molecules indicate that the samples have good chemisorption properties for CO_2 . Under continuous illumination, the key intermediates $^*\text{COOH}$ and $^*\text{CO}$ for the generation of CO are detected at 1328 , 1638 , and 1923 cm^{-1} . $^*\text{CHO}$, $^*\text{CH}_2\text{O}$, and $^*\text{CH}_3\text{O}$ at 1136 , 1197 , and 1434 cm^{-1} and several stretching vibrations belonging to the C-H bonds (CH_2 and CH_3) at $2800\text{--}3100\text{ cm}^{-1}$ are the critical intermediates for the generation of CH_4 . [57] In particular, $^*\text{COCO}$ located at 1913 cm^{-1} is the product of $^*\text{CO}$ coupling and likewise an essential precursor for the generation of C_2 products [58].

Based on the above analysis, we proposed a possible pathway for CO_2 reduction. Firstly, CO_2 dissolved in aqueous solution formed carbonates and bicarbonates or directly adsorbed on the catalyst surface and formed

CO_2^- species, which subsequently generated $^*\text{COOH}$ and $^*\text{CO}$ through hydrogenation reactions. Due to the good adsorption characteristics of Cu nanoparticles and dispersed Ni single-atom sites for $^*\text{CO}$, only a tiny portion of $^*\text{CO}$ was desorbed to form CO gaseous products. Most adsorbed state $^*\text{CO}$ will continue participating in the reduction reaction on the catalyst surface to generate CH_4 and C_2H_6 ultimately. The detection of $^*\text{CHO}$, $^*\text{CH}_2\text{O}$, $^*\text{CH}_3\text{O}$, $^*\text{CH}_2$, and $^*\text{CH}_3$ species on the CA/ $\text{Ni}_1\text{Cu}_{\text{NP}}$ N-C surfaces implies that CH_4 is generated via the formaldehyde pathway. For the evolutionary pathway of the C_2 product, the $^*\text{CO}$ intermediate would generate the $^*\text{COCO}$ key intermediate via the C-C coupling, followed by a multi-step hydrogenation reaction to generate C_2H_6 .

To further validate the charge transfer mechanism on CA/ $\text{Ni}_1\text{Cu}_{\text{NP}}$ N-C and the synergistic effect between Cu nanoparticles and Ni single-atom sites, theoretical calculations based on density functional theory (DFT) were performed (Fig. S19). As shown in Fig. 9a-b, the work functions of CA and $\text{Ni}_1\text{Cu}_{\text{NP}}$ N-C are 1.908 and 3.359 eV , respectively, which implies that the electrons located in CA will be transferred to $\text{Ni}_1\text{Cu}_{\text{NP}}$ N-C driven by the potential difference until a new stable Fermi energy level is established. The hybridization of CA and $\text{Ni}_1\text{Cu}_{\text{NP}}$ N-C can improve the carrier separation efficiency on CA and transport enough electrons to $\text{Ni}_1\text{Cu}_{\text{NP}}$ N-C to promote CO_2 catalytic reduction. Then, the electron difference densities (EDD) of CA/ Ni_1 N-C and CA/ $\text{Ni}_1\text{Cu}_{\text{NP}}$ N-C were calculated to further explore the charge separation mechanism. As shown in Fig. 9c-d, the charge at the heterojunction interface is depleted on the CA (green) surface and accumulated on the Ni_1 N-C/ $\text{Ni}_1\text{Cu}_{\text{NP}}$ N-C layer (blue). In particular, this charge transfer behavior is enhanced when Cu nanoparticles are introduced, suggesting that it can promote charge transfer and aggregation. Fig. S20 and Fig. 9e-f show the charge density distributions on the Ni_1 N-C and $\text{Ni}_1\text{Cu}_{\text{NP}}$ N-C cut layers, and it can be seen that the Ni centers have high charge densities, which facilitates the adsorption of the reactants/intermediates and the catalytic reactions with multi-electron participation. In the CA/ $\text{Ni}_1\text{Cu}_{\text{NP}}$ N-C system, the charge density around the electron-rich center Ni-N_4 shows an asymmetric distribution in the presence of Cu nanoparticles. This asymmetric active site is favorable for coupling adjacent $^*\text{CO}$, thus promoting the generation of C_2 products. [59,60] Finally, we calculated the density of states (DOS) of CA/ Ni_1 N-C and CA/ $\text{Ni}_1\text{Cu}_{\text{NP}}$ N-C. As shown in Fig. S21, CA/ $\text{Ni}_1\text{Cu}_{\text{NP}}$ N-C has a more vital and rightward-shifted DOS, which allows for stronger binding of reactants/intermediates on its surface [15].

3. Conclusion

In conclusion, we anchored Ni single-atom and Cu nanoparticle sites on nitrogen-doped carbon via a facile ion-exchange strategy and calcination, and subsequently hybridized it with CoAl-LDH based on ultrasonic self-assembly. The intermediates of the photocatalytic reactions were determined by in situ characterization techniques to speculate the possible CO_2 evolution pathways. The charge transfer mechanism on the

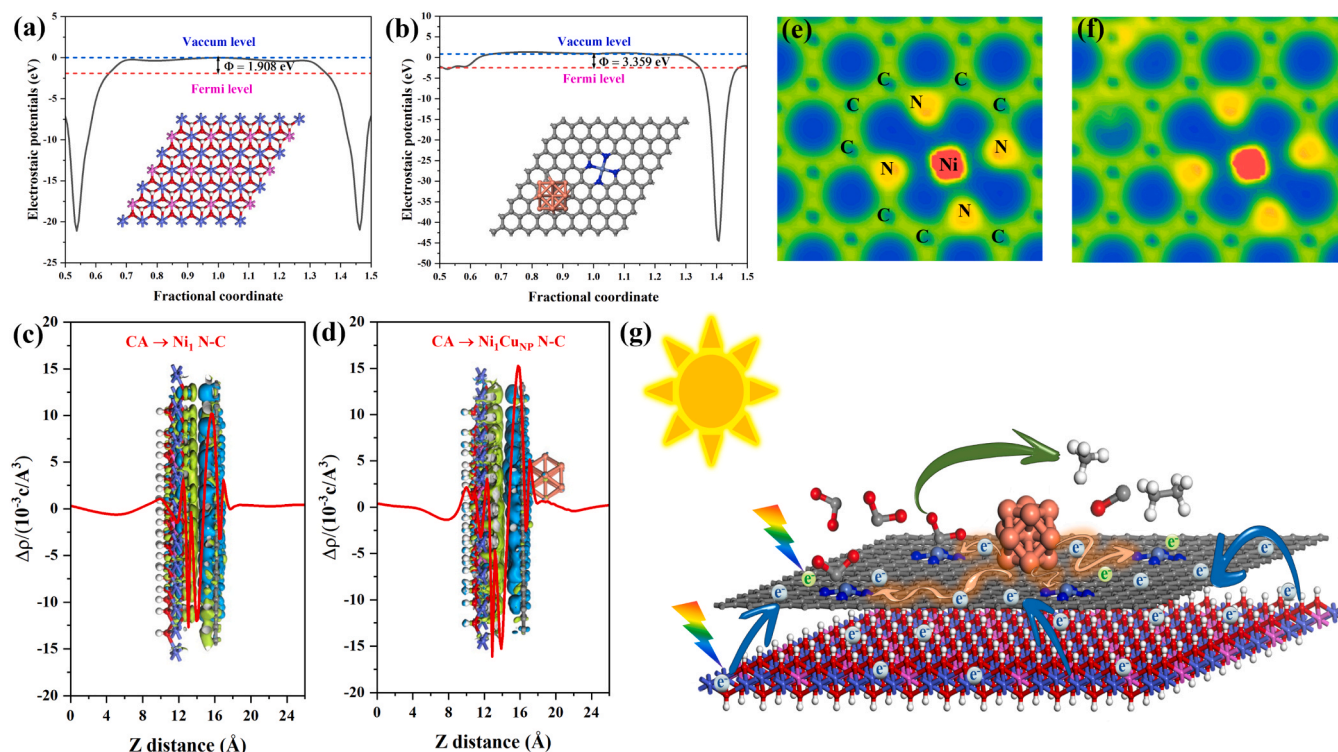


Fig. 9. The work functions of (a) CoAl-LDH and (b) Ni₁Cu_{NP} N-C. The electron difference densities of (c) CA/Ni₁ N-C and (d) CA/Ni₁Cu_{NP} N-C. The charge density distributions on the (e) Ni₁ N-C cut layers of CA/Ni₁ N-C and (f) Ni₁Cu_{NP} N-C cut layers of CA/Ni₁Cu_{NP} N-C. (g) The possible photocatalytic CO₂ reduction mechanism on CA/Ni₁Cu_{NP} N-C.

CA/Ni₁Cu_{NP} N-C and the potential synergistic interactions between Ni single atoms and Cu nanoparticles were explored in depth by DFT calculations. As shown in Fig. 9g, the photogenerated electrons located on CoAl-LDH will be transferred to N-C under the effect of the internal potential and ultimately gathered on the dispersed Ni single-atom sites, providing sufficient power for CO₂ reduction. The loading of Cu nanoparticles can significantly promote charge transfer. In addition, it can change the charge density distribution on N-C to create asymmetric Ni-N₄ sites, enhancing key intermediates' adsorption. As a result, the yields of CH₄ and C₂H₆ for the best samples were 35.245 and 25.328 μmol g⁻¹ h⁻¹ with electron selectivity of 40.24% and 50.61%, respectively.

3.1. Experimental procedures

Detailed descriptions of the preparation processes, characterization techniques, photoelectrochemical tests, photocatalytic CO₂ reduction performance tests, and DFT calculation setup are available in the [Supplementary Information](#).

CRediT authorship contribution statement

Wei-guo Pan: Writing – review & editing, Investigation, Supervision. **Chu-fan Li:** Investigation, Writing – original draft. **Zhen-rui Zhang:** Writing – review & editing. **Tong Wu:** Writing – review & editing. **Rui-tang Guo:** Conceptualization, Writing – review & editing, Supervision.

Declaration of Competing Interest

The authors declare that they have no known competing financial interests or personal relationships that could have appeared to influence the work reported in this paper.

Data availability

Data will be made available on request.

Acknowledgments

This work was financially supported by the Natural Science Foundation of Shanghai (23ZR1424500) and the Shanghai Local University Capacity Building Project (22010501500).

Appendix A. Supporting information

Supplementary data associated with this article can be found in the online version at [doi:10.1016/j.apcatb.2023.123492](https://doi.org/10.1016/j.apcatb.2023.123492).

References

- [1] J. Yu, L. Huang, Q. Tang, S. Yu, Q. Qi, J. Zhang, D. Ma, Y. Lei, J. Su, Y. Song, J. Eloi, R.L. Harniman, U. Borucu, L. Zhang, M. Zhu, F. Tian, L. Du, D.L. Phillips, I. Manners, R. Ye, J. Tian, Artificial spherical chromatophore nanomicelles for selective CO₂ reduction in water, *Nat. Catal.* 6 (2023) 464–475.
- [2] S. Wang, X. Han, Y. Zhang, N. Tian, T. Ma, H. Huang, Inside-and-out semiconductor engineering for CO₂ photoreduction: from recent advances to new trends, *Small Struct.* 2 (2020) 2000061.
- [3] Q.S. Wang, Y.C. Yuan, C.F. Li, Z.R. Zhang, C. Xia, W.G. Pan, R.T. Guo, Research progress on photocatalytic CO₂ reduction based on perovskite oxides, *Small* (2023), e2301892.
- [4] Z. Liu, Z. Chen, M. Li, J. Li, W. Zhuang, X. Yang, S. Wu, J. Zhang, Construction of single Ni atom-immobilized ZIF-8 with ordered hierarchical pore structures for selective CO₂ photoreduction, *ACS Catal.* 13 (2023) 6630–6640.
- [5] X. Chen, R. Guo, W. Pan, Y. Yuan, X. Hu, Z. Bi, J. Wang, A novel double S-scheme photocatalyst Bi₇O₉I₃/Cd_{0.5}Zn_{0.5}S QDs/WO_{3-x} with efficient full-spectrum-induced phenol photodegradation, *Appl. Catal. B Environ.* 318 (2022), 121839.
- [6] H. Ou, G. Li, W. Ren, B. Pan, G. Luo, Z. Hu, D. Wang, Y. Li, Atomically dispersed Au-assisted C-C coupling on red phosphorus for CO₂ photoreduction to C₂H₆, *J. Am. Chem. Soc.* 144 (2022) 22075–22082.
- [7] B.N. Choi, J.Y. Seo, Z. An, P.J. Yoo, C.H. Chung, An in-situ spectroscopic study on the photochemical CO₂ reduction on CsPbBr₃ perovskite catalysts embedded in a porous copper scaffold, *Chem. Eng. J.* 430 (2022), 132807.

- [8] X. Wu, R. Zhong, X. Lv, Z. Hu, D. Xia, C. Li, B. Song, S. Liu, Modulating g-C₃N₄-based van der Waals heterostructures with spatially separated reductive centers for tandem photocatalytic CO₂ methanation, *Appl. Catal. B Environ.* 330 (2023), 122666.
- [9] R.T. Guo, Z.R. Zhang, C. Xia, C.F. Li, W.G. Pan, Recent progress of cocatalysts loaded on carbon nitride for selective photoreduction of CO₂ to CH₄, *Nanoscale* 15 (2023) 8548–8577.
- [10] Z.H. Xue, D. Luan, H. Zhang, X.W. Lou, Single-atom catalysts for photocatalytic energy conversion, *Joule* 6 (2022) 92–133.
- [11] C.F. Li, W.G. Pan, Z.R. Zhang, T. Wu, R.T. Guo, Recent progress of single-atom photocatalysts applied in energy conversion and environmental protection, *Small* 19 (2023), e2300460.
- [12] X. Xiong, C. Mao, Z. Yang, Q. Zhang, G.I.N. Waterhouse, L. Gu, T. Zhang, Photocatalytic CO₂ reduction to CO over Ni single atoms supported on defect-rich zirconia, *Adv. Energy Mater.* 10 (2020) 2002928.
- [13] D. Liu, J.C. Li, S. Ding, Z. Lyu, S. Feng, H. Tian, C. Huyen, M. Xu, T. Li, D. Du, P. Liu, M. Shao, Y. Lin, 2D single-atom catalyst with optimized iron sites produced by thermal melting of metal–organic frameworks for oxygen reduction reaction, *Small Methods* 4 (2020) 1900827.
- [14] G.P. Lu, H. Shan, Y. Lin, K. Zhang, B. Zhou, Q. Zhong, P. Wang, A Fe single atom on N,S-doped carbon catalyst for performing N-alkylation of aromatic amines under solvent-free conditions, *J. Mater. Chem. A* 9 (2021) 25128–25135.
- [15] A. Deng, E. Zhao, Q. Li, Y. Sun, Y. Liu, S. Yang, H. He, Y. Xu, W. Zhao, H. Song, Z. Xu, Z. Chen, Atomic cobalt–silver dual-metal sites confined on carbon nitride with synergistic Ag nanoparticles for enhanced CO₂ photoreduction, *ACS Nano* 17 (2023) 11869–11881.
- [16] Z. Chen, G. Zhang, Q. Hu, Y. Zheng, S. Cao, G. Chen, C. Li, T. Boyko, N. Chen, W. Chen, T. Regier, J. Dynes, J. Wang, H.-T. Wang, J. Zhou, S. Sun, The deep understanding into the promoted carbon dioxide electroreduction of ZIF-8-derived single-atom catalysts by the simple grinding process, *Small Struct.* 3 (2022) 2200031.
- [17] C. Wang, Y. Chen, M. Zhong, T. Feng, Y. Liu, S. Feng, N. Zhang, L. Shen, K. Zhang, B. Yang, Hollow mesoporous carbon nanocages with Fe isolated single atomic site derived from a MOF/polymer for highly efficient electrocatalytic oxygen reduction, *J. Mater. Chem. A* 9 (2021) 22095–22101.
- [18] Y. Liu, X. Wu, Z. Li, J. Zhang, S.X. Liu, S. Liu, L. Gu, L.R. Zheng, J. Li, D. Wang, Y. Li, Fabricating polyoxometalates-stabilized single-atom site catalysts in confined space with enhanced activity for alkynes diboration, *Nat. Commun.* 12 (2021) 4205.
- [19] H. Liu, M. Cheng, Y. Liu, J. Wang, G. Zhang, L. Li, L. Du, G. Wang, S. Yang, X. Wang, Single atoms meet metal–organic frameworks: collaborative efforts for efficient photocatalysis, *Energy Environ. Sci.* 15 (2022) 3722–3749.
- [20] G. Jia, M. Sun, Y. Wang, Y. Shi, L. Zhang, X. Cui, B. Huang, J.C. Yu, Asymmetric coupled dual-atom sites for selective photoreduction of carbon dioxide to acetic acid, *Adv. Funct. Mater.* 32 (2022) 2206817.
- [21] W. Xu, H. Tang, H. Gu, H. Xi, P. Wu, B. Liang, Q. Liu, W. Chen, Research progress of asymmetrically coordinated single-atom catalysts for electrocatalytic reactions, *J. Mater. Chem. A* 10 (2022) 14732–14746.
- [22] L. Zeng, C. Xue, Single metal atom decorated photocatalysts: progress and challenges, *Nano Res.* 14 (2020) 934–944.
- [23] C. Gao, J. Low, R. Long, T. Kong, J. Zhu, Y. Xiong, Heterogeneous single-atom photocatalysts: Fundamentals and applications, *Chem. Rev.* 120 (2020) 12175–12216.
- [24] C. Tang, Y. Jiao, B. Shi, J.N. Liu, Z. Xie, X. Chen, Q. Zhang, S.Z. Qiao, Coordination tunes selectivity: two-electron oxygen reduction on high-loading molybdenum single-atom catalysts, *Angew. Chem. Int. Ed.* 59 (2020) 9171–9176.
- [25] B. Wang, M. Li, S. Zhang, H. Wu, Y. Liao, H. Li, Synergistic effect between Co single atoms and nanoparticles enables selective synthesis of bio-based benzimidazoles, *Appl. Catal. B Environ.* 327 (2023), 122454.
- [26] C. Zhu, Y. Shen, F. Yang, P. Zhu, C. An, Engineering hydrogenated TiO₂ nanosheets by rational deposition of Ni clusters and Pt single atoms onto exposing facets for high-performance solar fuel production, *Chem. Eng. J.* 466 (2023), 143174.
- [27] G. Meng, J. Sun, L. Tao, K. Ji, P. Wang, Y. Wang, X. Sun, T. Cui, S. Du, J. Chen, D. Wang, Y. Li, Ru₁Co_n single-atom alloy for enhancing fischer–tropsch synthesis, *ACS Catal.* 11 (2021) 1886–1896.
- [28] W. Ren, X. Tan, C. Jia, A. Krammer, Q. Sun, J. Qu, S.C. Smith, A. Schueler, X. Hu, C. Zhao, Electronic regulation of nickel single atoms by confined nickel nanoparticles for energy-efficient CO₂ electroreduction, *Angew. Chem. Int. Ed. Engl.* 61 (2022), e20220335.
- [29] J. Li, L.-W. Chen, Y.-C. Hao, M. Yuan, J. Lv, A. Dong, S. Li, H. Gu, A.-X. Yin, W. Chen, P. Li, B. Wang, Asymmetric coordinated single-atom Pd sites for high performance CO₂ electroreduction and Zn–CO₂ battery, *Chem. Eng. J.* 461 (2023), 141865.
- [30] X. Xiong, Y. Zhao, R. Shi, W. Yin, Y. Zhao, G.I.N. Waterhouse, T. Zhang, Selective photocatalytic CO₂ reduction over Zn-based layered double hydroxides containing tri or tetravalent metals, *Sci. Bull.* 65 (2020) 987–994.
- [31] Y. Yang, J. Wu, T. Xiao, Z. Tang, J. Shen, H. Li, Y. Zhou, Z. Zou, Urchin-like hierarchical CoZnAl-LDH/RGO/g-C₃N₄ hybrid as a Z-scheme photocatalyst for efficient and selective CO₂ reduction, *Appl. Catal. B Environ.* 255 (2019), 117771.
- [32] S. Zhang, Y. Rong, J. Wei, Z. Li, T. Liang, Z. Yu, H. Zhu, S. Wang, Y. Hou, Flower-like microspheres Z-scheme Bi₂Sn₂O₇/NiAl-LDH heterojunction for boosting photocatalytic CO₂ reduction under visible light, *J. Colloid Interf. Sci.* 629 (2023) 604–615.
- [33] J. Tao, X. Yu, Q. Liu, G. Liu, H. Tang, Internal electric field induced S-scheme heterojunction MoS₂/CoAl LDH for enhanced photocatalytic hydrogen evolution, *J. Colloid Interf. Sci.* 585 (2021) 470–479.
- [34] Y. Lu, D. Wu, Y. Qin, Y. Xie, Y. Ling, H. Ye, Y. Zhang, Facile construction of BiOBr/CoAl-LDH heterojunctions with suppressed Z-axis growth for efficient photoreduction of CO₂, *Sep. Purif. Technol.* 302 (2022), 122090.
- [35] C. Xia, R. Guo, Z. Bi, Z. Zhang, C. Li, W. Pan, A dual Z-scheme heterojunction Cu-CuTCP/Cu₂O/CoAl-LDH for photocatalytic CO₂ reduction to C₁ and C₂ products, *Dalton Trans.* 52 (2023) 12742–12754.
- [36] H. Wu, T. He, M. Dan, L. Du, N. Li, Z.-Q. Liu, Activated Ni-based metal–organic framework catalyst with well-defined structure for electrosynthesis of hydrogen peroxide, *Chem. Eng. J.* 435 (2022), 134863.
- [37] Y. Hou, Y.-L. Liang, P.-C. Shi, Y.-B. Huang, R. Cao, Atomically dispersed Ni species on N-doped carbon nanotubes for electroreduction of CO₂ with nearly 100% CO selectivity, *Appl. Catal. B Environ.* 271 (2020), 118929.
- [38] C. Shao, L. Wu, Y. Wang, K. Qu, H. Chu, L. Sun, J. Ye, B. Li, X. Wang, An open superstructure of hydrangea-like carbon with highly accessible Fe-N₄ active sites for enhanced oxygen reduction reaction, *Chem. Eng. J.* 429 (2022), 132307.
- [39] D.L. Meng, M.D. Zhang, D.H. Si, M.J. Mao, Y. Hou, Y.B. Huang, R. Cao, Highly selective tandem electroreduction of CO₂ to ethylene over atomically isolated nickel-nitrogen site/copper nanoparticle catalysts, *Angew. Chem. Int. Ed. Engl.* 60 (2021) 25485–25492.
- [40] C.F. Li, R.T. Guo, Z.R. Zhang, T. Wu, Y.L. Liu, Z.C. Zhou, M. Aisanjiang, W.G. Pan, Constructing CoAl-LDO/MoO_{3-x} S-scheme heterojunctions for enhanced photocatalytic CO₂ Reduct., *J. Colloid Interf. Sci.* 650 (2023) 983–993.
- [41] C. Li, R. Guo, Z. Zhang, T. Wu, C. Yue, W. Pan, Loading metal nanoparticles on the CoAl-LDH/CGCNN S-scheme heterojunction for efficient photocatalytic CO₂ reduction under visible light, *Sep. Purif. Technol.* 322 (2023), 124266.
- [42] J. Huo, X. Cao, Y. Tian, L. Li, J. Qu, Y. Xie, X. Nie, Y. Zhao, J. Zhang, H. Liu, Atomically dispersed Mn atoms coordinated with N and O within an N-doped porous carbon framework for boosted oxygen reduction catalysis, *Nanoscale* 15 (2023) 5448–5457.
- [43] S. Yuan, J. Zhang, L. Hu, J. Li, S. Li, Y. Gao, Q. Zhang, L. Gu, W. Yang, X. Feng, B. Yang, Decarboxylation-induced defects in MOF-derived single cobalt atom@carbon electrocatalysts for efficient oxygen reduction, *Angew. Chem. Int. Ed. Engl.* 60 (2021) 21685–21690.
- [44] H. Yang, P. Zhang, X. Yi, C. Yan, D. Pang, L. Chen, S. Wang, C. Wang, B. Liu, G. Zhang, Z. Zhou, X. Li, Constructing highly utilizable Fe-N₄ single-atom sites by one-step gradient pyrolysis for electroreduction of O₂ and CO₂, *Chem. Eng. J.* 440 (2022), 135749.
- [45] L. Hu, A. He, X. Shen, Q. Gu, J. Zheng, Z. Wu, Y. Jiang, X. Wang, J. Xu, Y. Kan, F. Xu, A high-efficiency zirconium-based single-atom catalyst for the transformation of biomass-derived 5-hydroxymethylfurfural to 2,5-bis(hydroxymethyl)furan with nearly 100% selectivity, *Green. Chem.* 24 (2022) 6931–6944.
- [46] J. Yang, H.-Q. Chen, F. Qiao, X. Zhu, T. Wang, W.-P. Pan, Engineering single-atom Pd sites in ZIF-derived porous Co₃O₄ for enhanced elementary mercury removal, *Sep. Purif. Technol.* 309 (2023), 123050.
- [47] C.F. Li, R.T. Guo, T. Wu, W.G. Pan, Progress and perspectives on 1D nanostructured catalysts applied in photo(electro)catalytic reduction of CO₂, *Nanoscale* 14 (2022) 16033–16064.
- [48] C.F. Li, R.T. Guo, Z.R. Zhang, T. Wu, W.G. Pan, Converting CO₂ into value-added products by Cu₂O-based catalysts: from photocatalysis, electrocatalysis to photoelectrocatalysis, *Small* 19 (2023), e2207875.
- [49] S. Ma, Z. Han, K. Leng, X. Liu, Y. Wang, Y. Qu, J. Bai, Ionic exchange of metal–organic frameworks for constructing unsaturated copper single-atom catalysts for boosting oxygen reduction reaction, *Small* 16 (2020), e2001384.
- [50] G. Hwa Jeong, Y. Chuan Tan, J. Tae Song, G.-Y. Lee, H. Jin Lee, J. Lim, H. Young Jeong, S. Won, J. Oh, S. Ouk, Kim, Synthetic multiscale design of nanostructured Ni single atom catalyst for superior CO₂ electroreduction, *Chem. Eng. J.* 426 (2021), 131063.
- [51] J. Bai, W. Ge, P. Zhou, P. Xu, L. Wang, J. Zhang, X. Jiang, X. Li, Q. Zhou, Y. Deng, Precise constructed atomically dispersed Fe/Ni sites on porous nitrogen-doped carbon for oxygen reduction, *J. Colloid Interf. Sci.* 616 (2022) 433–439.
- [52] Z. Li, D. He, X. Yan, S. Dai, S. Younan, Z. Ke, X. Pan, X. Xiao, H. Wu, J. Gu, Size-dependent nickel-based electrocatalysts for selective CO₂ reduction, *Angew. Chem. Int. Ed. Engl.* 59 (2020) 18572–18577.
- [53] X. Yang, J. Cheng, H. Lv, X. Yang, L. Ding, Y. Xu, K. Zhang, W. Sun, J. Zhou, Sulfur-doped unsaturated Ni-N₃ coordination for efficient electroreduction of CO₂, *Chem. Eng. J.* 450 (2022), 137950.
- [54] C. Wang, L. Kuai, W. Cao, H. Singh, A. Zakharov, Y. Niu, H. Sun, B. Geng, Highly dispersed Cu atoms in MOF-derived N-doped porous carbon inducing Pt loads for superior oxygen reduction and hydrogen evolution, *Chem. Eng. J.* 426 (2021), 130749.
- [55] W. Zhu, J. Fu, J. Liu, Y. Chen, X. Li, K. Huang, Y. Cai, Y. He, Y. Zhou, D. Su, J.-J. Zhu, Y. Lin, Tuning single atom-nanoparticle ratios of Ni-based catalysts for synthesis gas production from CO₂, *Appl. Catal. B Environ.* 264 (2020), 118502.
- [56] X. Yang, X. Lan, Y. Zhang, H. Li, G. Bai, Rational design of MoS₂@COF hybrid composites promoting C-C coupling for photocatalytic CO₂ reduction to ethane, *Appl. Catal. B Environ.* 325 (2023), 122393.
- [57] F. Xu, Z. Li, R. Zhu, Y. Chu, Z. Pan, S. Xia, J. Fu, Z. Xiao, X. Ji, M. Liu, B. Weng, Narrow band-gapped perovskite oxysulfide for CO₂ photoreduction towards ethane, *Appl. Catal. B Environ.* 316 (2022), 121615.

- [58] S. Xie, Y. Li, B. Sheng, W. Zhang, W. Wang, C. Chen, J. Li, H. Sheng, J. Zhao, Self-reconstruction of paddle-wheel copper-node to facilitate the photocatalytic CO₂ reduction to ethane, *Appl. Catal. B Environ.* 310 (2022), 121320.
- [59] H. Shi, H. Wang, Y. Zhou, J. Li, P. Zhai, X. Li, G.G. Gurzadyan, J. Hou, H. Yang, X. Guo, Atomically dispersed indium-copper dual-metal active sites promoting C-C coupling for CO₂ photoreduction to ethanol, *Angew. Chem. Int. Ed. Engl.* 61 (2022), e202208904.
- [60] Y. Wang, Q. Wang, J. Wu, X. Zhao, Y. Xiong, F. Luo, Y. Lei, Asymmetric atomic sites make different: recent progress in electrocatalytic CO₂ reduction, *Nano Energy* 103 (2022), 107815.